Numerical study of hot and cold spheroidal particles in a viscous fluid

Mohammad Majlesara[a], Omid Abouali[a,*], Reza Kamali[a], Mehdi Niazi Ardekani[b], Luca Brandt[b]

[a] School of Mechanical Engineering, Shiraz University, Mollasadra Street, Shiraz 71348-51154, Iran
[b] Linné Flow Centre and SeRC (Swedish e-Science Research Centre), KTH Mechanics, Stockholm SE-10044, Sweden

A B S T R A C T

The gravity-driven motion of rigid particles with a temperature difference with respect to the surrounding viscous fluid is relevant in many natural and industrial processes, yet this has mainly been investigated for spherical particles. In this work we study the influence of the Grashof number (Gr) on the settling velocity and the drag coefficient C_D of a single spheroidal particle of different aspect ratios (1/3, 1 and 3). The discrete forcing immersed boundary method (IBM) is employed to represent the fluid-solid interaction in both momentum and temperature equations, while the Boussinesq approximation is used for the coupling of momentum and temperature. The simulations show that the drag coefficient of any spheroidal particle below the onset of secondary motion can be predicted by the results of the settling spheres at the desired Grashof number as the main effect of the particle shape at low Galileo number (Ga) and sufficiently small Gr/Ga^2 is found to be the change in the frontal area of the particle. Furthermore, we identify the regions of stable sedimentation (vertical path) in the $Ga - Gr/Ga^2$ plane for the 3 particle shapes, investigated in this study. We show that the critical Ga beyond which the particle exhibits the zigzagging motion, is considerably smaller for oblate particles in comparison to prolate ones at low Gr/Ga^2. However, both spheroidal shapes indicate a similar behavior as Gr/Ga^2 increases beyond 0.5.

© 2019 Elsevier Ltd. All rights reserved.

1. Introduction

Freely moving particles under gravity in a viscous quiescent fluid can be found in many environmental, biological and industrial applications such as dispersion of soot particles in air, settling of micro-organisms in oceans and fluidization of solid particles in chemical reactors. In such applications, a wide range of parameters affect the sedimentation of solid particles. Among those, the particle shape and the temperature difference with respect to the surrounding fluid are emphasized in this work as they have a critical role on the overall flow pattern. The particle wake is affected in the latter due to the Buoyancy force that causes natural convection. Accounting for these two parameters is crucial to provide more reliable and realistic predictions. However, this parameter area is barely covered in the literature and most of the numerical studies conducted on this topic are limited to particles of spherical shape [1–3]. This is mainly due to the complexity of 3*D* numerical algorithms that are able to fully resolve the hydrodynamic and thermal interaction between the fluid and the solid phases with different shapes. Hence, the main objective of the current study is to investigate settling non-spherical particles in the presence of heat transfer and compare the results among the cases with different shapes and thermal conditions. The understanding of such complex phenomena is of utmost importance for improving the current models and is crucial for a better design of related thermo-mechanical systems.

Due to the complexity of particulate flows induced by natural or mixed convection, the earlier numerical and experimental studies used simpler theoretical approaches to investigate these challenging physical phenomena. Most of these studies investigated a single stationary particle of circular (2*D*) or spherical (3*D*) shape at low Reynolds (*Re*) and Grashof (*Gr*) numbers [4–7], while only a few reported information about non-spherical particles [8,9]. With the rapid increase of the computational power and efficient numerical algorithms, fully-resolved methods for the detailed simulations of moving particles with heat transfer at higher *Re* and *Gr* numbers have become available. Gan et al. [10] used the boundary fitted approach to perform direct numerical simulations (*DNS*) of the heat transfer of 2*D* solid particles, settling in a fluid at moderate Reynolds numbers (*Re* < 100). They found that the particle is oscillating or migrating towards the wall at various *Gr*. Recently, efficient numerical algorithms with non-boundary fitted approaches have significantly reduced the computational cost of

such simulations. Yu et al. [1] presented a new combination of energy equation with distributed Lagrange-multiplier/fictitious domain (*DLM/FD*) method to study the motion of circular particles with fixed and uniform temperatures. They analyzed the motion of a catalyst particle and investigated the effect of Peclet and Reynolds numbers on the heat conductivities of nano-fluids and sheared non-colloidal suspensions. An immersed boundary method (*IBM*) was employed by Feng and Michaelides [2] to study the motion and heat transfer of hotter or colder circular particles at significantly larger Reynolds and Grashof numbers. They found that the drag coefficient of non-isothermal particles strongly depends on the Grashof number at low and moderate Reynolds numbers. According to this study, the hotter and colder particles experience more and less drag force, respectively, due to the heat transfer between the solid and the fluid phase. Dan and Wachs [3] extended the *DLM/FD* approach to investigate the heat transfer of 3*D* particles for the first time. These authors obtained a similar physical trend as in the 2*D* results. To get more insight into the natural convection flows, Wachs [11] extended their previous work by investigating various particulate flow cases. In particular, he examined a 3*D* spherical catalyst rising in an enclosure, due to natural convection, while being heavier than the suspending fluid. Hashemi et al. [12] employed the Lattice Boltzmann method (*LBM*) to investigate the effects of Reynolds, Prandtl and Grashof numbers on the sedimentation of an isolated spherical particle with a fixed or varying temperature. These authors also performed simulations of 30 hot spherical particles settling in an enclosure and studied the hydraulic and heat transfer interactions with the surrounding fluid. Xu et al. [13] further showed the application of *LBM* to study transport phenomena in multiphase flows. Recently, Eshghinejadfard and Thevenin [14] combined the thermal *IBM* with *LBM* to resolve the interactions between circular/spherical particles and the fluid in the presence of heat transfer among the two phases.

Although the physical understanding of the heat transfer in particulate flows has been significantly improved in recent years, these findings are mostly restricted to the particles with a spherical shape and only a few studies are devoted to the shape effect. Among these studies, Tavassoli et al. [15] and He and Tafti [16] numerically investigated the heat transfer in flow through fixed random arrays of non-spherical particles. Xu et al. [17] performed particle-resolved direct numerical simulations to study the motion of elliptical particles in the presence of heat transfer for the first time. They analyzed the sedimentation of cold and hot elliptic particles in a viscous fluid and found three additional settling modes arising from thermal effects. Walayat et al. [18] further studied the effects of the fluid thermal properties on the sedimentation of elliptic particles under different thermal conditions via the multigrid finite-element fictitious boundary method. These authors revisited the case study of Xu et al. [17] and found a new settling mode for a hot elliptical particle. They concluded that the trajectory and the orientation of the settling particle depends on the Grashof number and the density ratio as well as on the other physical properties of the fluid.

Despite all studies on this subject, fully resolved simulations of heat transfer of moving 3*D* non-spherical particles are still missing in the literature. Therefore, in this work we perform direct numerical simulations of free-falling spheroidal particles with fixed temperature in a viscous fluid and compare the results with the data obtained for spherical particles. For this purpose, we have extended the immersed boundary method (*IBM*) in [19] to account for the heat transfer in the presence of non-spherical particles with fixed temperature. The numerical code has been previously used to study the settling of spherical and spheroidal particles in quiescent fluids [20–22] and the heat transfer in particle suspensions [23,24]. We hope that this study lays the ground for further pa-

rameter studies in this complex subject, such as the effect of heat capacity and conductivity ratio.

The paper is organized as follows. The governing equations and the numerical implementations are explained in Section 2, followed by a validation study in Section 3. The results of the numerical simulations are discussed in Section 4 and the final conclusions and remarks are drawn in Section 5.

2. Methodology

Uhlmann [25] developed a computationally efficient *IBM* to fully resolve particle-laden flows. Breugem [19] introduced improvements to this method, making it second order accurate in space while increasing the numerical stability for mass density ratios (particle over fluid density ratio) near unity [see also 26]. Ardekani et al. [20] extended this method to account for non-spherical particles and heat transfer in particulate flows [23,24]. In this work we use the same numerical code to study the free falling spheroidal particles with constant temperature in a viscous fluid. *IBM* is used here to represent particles in both momentum and temperature equations [27].

2.1. Governing equations

The non-dimensional equations below describe the momentum and heat transfer in particulate flows with a constant temperature assumed on the surface of the particles:

$$\frac{\partial \mathbf{u}}{\partial t} + \nabla \cdot \mathbf{u} \otimes \mathbf{u} = -\nabla p + \frac{1}{Re}\nabla^2\mathbf{u} - \frac{Gr}{Re^2}T\hat{\mathbf{e}}_g + \mathbf{f}, \tag{1}$$

$$\frac{\partial T}{\partial t} + \mathbf{u}\cdot\nabla T = \frac{1}{Pr\,Re}\nabla^2 T + S_T, \tag{2}$$

$$\nabla \cdot \mathbf{u} = 0, \tag{3}$$

with $\mathbf{u}$ the fluid velocity, p the pressure, T the temperature and $\hat{\mathbf{e}}_g$ denoting the unit vector in the gravity direction. *Re, Gr* and *Pr* are the Reynolds, Grashof and Prandtl numbers, defined below. The extra terms $\mathbf{f}$ and S_T on the right hand side of the equations are the source terms, given by IBM and active in the immediate vicinity of the particles to enforce the boundary conditions at the surface. The non-dimensional temperature T in the equations above is normalized with the two reference temperatures $\tilde{\Theta}_p$ and $\tilde{\Theta}_f$ ($T = (\Theta - \tilde{\Theta}_f)/(\tilde{\Theta}_p - \tilde{\Theta}_f)$). $\tilde{\Theta}_p$ and $\tilde{\Theta}_f$ are the initial temperatures of the particles and the fluid phase, respectively. The Boussinesq approximation is used here to account for the effect of temperature variation on the flow field. The influence of temperature on the properties of fluid medium is assumed negligible, except for the density in the gravitational term which has the form:

$$\rho_B = \rho_f\big[1 - \beta_f\big(\Theta - \tilde{\Theta}_f\big)\big], \tag{4}$$

where β_f represents the fluid thermal expansion coefficient and ρ_f denotes the fluid density at $\Theta = \tilde{\Theta}_f$. The Boussinesq approximation contribute to the momentum transfer in the gravity direction via GrT/Re^2 on the right hand side of the non-dimensional Navier-Stokes equations.

The non-dimensional parameters defining the problem are the density ratio ρ_r, Grashof number *Gr*, Prandtl number *Pr* and Galileo number *Ga*. These parameters are defined as follows:

$$\rho_r \equiv \frac{\rho_p}{\rho_f} \quad \& \quad Gr \equiv \frac{\rho_f^2\beta_f D_{eq}^3 g(\tilde{\Theta}_p - \tilde{\Theta}_f)}{\mu^2} \quad \& \quad Pr \equiv \frac{\mu C_{pf}}{k_f}$$
$$\& \quad Ga \equiv \sqrt{\frac{\rho_f^2|\rho_r-1|gD_{eq}^3}{\mu^2}}, \tag{5}$$

where the subscripts $_f$ and $_p$ denote the fluid phase and the particle phase. μ, C_{pf} and k_f are the dynamic viscosity, heat capacity

and heat conductivity of the fluid. g is the gravitational acceleration and D_{eq} is the equivalent diameter of a sphere with the same volume as the particle.

D_{eq} is considered as the reference length and a reference velocity U_{ref} is defined similarly to Dan and Wachs [3]. Therefore, the convective time scale D_{eq}/U_{ref} is employed to nondimensionalize time. The reference velocity U_{ref} is calculated from a balance between inertial and buoyancy forces:

$$U_{ref} = \sqrt{\frac{4D_{eq}}{3}(\rho_r - 1)g}. \tag{6}$$

The Reynolds number of the flow, calculated based on U_{ref} and D_{eq} is denoted by Re_{ref}:

$$Re_{ref} \equiv \frac{\rho_f U_{ref} D_{eq}}{\mu} = \frac{2\sqrt{3}}{3}Ga. \tag{7}$$

It should be noted that the coefficient $2\sqrt{3}/3$ is used in the definition of U_{ref} for a better comparison with the results in the literature [3,11]. An additional Reynolds number (Re_t) based on the particle terminal velocity, U_t, is also defined in this study to present the results. Note that the terminal Reynolds number is different than Re_{ref}.

The motion of rigid spheroidal particles are described by Newton-Euler Lagrangian equations,

$$\rho_p V_p \frac{d\mathbf{U}_p}{dt} = \oint_{\partial S_p} \boldsymbol{\tau} \cdot \mathbf{n} dA + \int_{V_p} (\rho_p - \rho_B)\mathbf{g} + \mathbf{F}_c, \tag{8}$$

$$\frac{d(\mathbf{I}_p \boldsymbol{\Omega}_p)}{dt} = \oint_{\partial S_p} \mathbf{r} \times (\boldsymbol{\tau} \cdot \mathbf{n}) dA - \int_{V_p} \mathbf{r} \times \rho_B \mathbf{g} + \mathbf{T}_c, \tag{9}$$

where $\mathbf{U}_p$ and $\boldsymbol{\Omega}_p$ are the particle translational and the angular velocity. ρ_p, V_p and $\mathbf{I}_p$ are the mass density, volume and moment-of-inertia tensor of a spheroidal particle. Here, $\mathbf{r}$ indicates the position vector with respect to the center of the spheroid and $\mathbf{n}$ is the outward unit normal vector at the particle surface ∂S_p where the stress tensor $\boldsymbol{\tau} = -p\mathbf{I} + \mu_f(\nabla\mathbf{u} + \nabla\mathbf{u}^T)$, acting on the surface of the particle is integrated. The volume integration of force term $(\rho_p - \rho_B)\mathbf{g}$ account for buoyancy and gravity forces, acting on the particles. $\mathbf{F}_c$ and $\mathbf{T}_c$ are the force and torque resulting from particle-particle (particle-wall) collisions.

2.2. Numerical algorithm

A brief summary of the employed numerical scheme is given here; more details and validations can be found in [19–21,27,28]. In this method the flow field is resolved on a uniform ($\Delta x = \Delta y = \Delta z$), staggered, Cartesian grid while particles are represented by a set of Lagrangian points, uniformly distributed on the surface of each particle. The number of Lagrangian grid points N_L on the surface of each particle is defined such that the Lagrangian grid volume ΔV_l becomes equal to the volume of the Eulerian mesh Δx^3, where the Lagrangian grid volume is defined by assuming a particle as a shell with thickness Δx. The Eqs. (1) and (2) are discretized using a second order central finite-difference scheme, except for the temperature advection term in Eq. (2) where the fifth-order weighted essentially non-oscillatory (*WENO*) scheme is applied ([29,30]). An explicit third-order Runge-Kutta scheme ([31]) is used for the time integration of all terms except the pressure gradient in the Navier-Stokes equations. For the latter the Crank-Nicolson scheme is used. The advancement of the solution is performed via the pressure-correction scheme used in [19] to project the velocity field in the divergence-free space.

The *IBM* source terms $\mathbf{f}$ and S_T on the right hand side of Eqs. (1) and (2) are obtained by spreading the source points $\mathbf{F}_l$ and

S_l from the Lagrangian to the Eulerian grid, using the regularized Dirac delta function δ_d of Roma et al. [32]:

$$\mathbf{f}\Big|_{ijk} = \sum_{l=1}^{N_L} \mathbf{F}_l \delta_d(\mathbf{x}_{ijk} - \mathbf{X}_l)\Delta V_l \tag{10}$$

$$S_T\Big|_{ijk} = \sum_{l=1}^{N_L} S_l \delta_d(\mathbf{x}_{ijk} - \mathbf{X}_l)\Delta V_l \tag{11}$$

with the *multi-direct forcing* scheme [33] employed to iteratively determine the *IBM* source term with a better accuracy.

The point force $\mathbf{F}_l$ is calculated at each Lagrangian point using the difference between the particle surface velocity ($\mathbf{U}_p + \boldsymbol{\Omega}_p \times \mathbf{r}$) and the interpolated first prediction velocity at the same point, while S_l is obtained based on the difference between the particle surface temperature and the interpolated prediction temperature. The first prediction velocity and the prediction temperature are computed by advancing Eqs. (1) and (2) in time without considering the IBM source terms $\mathbf{f}$ and S_T.

Accounting for the inertia of the fictitious fluid phase inside the particle volume, Eqs. (8) and (9) are rewritten as:

$$\rho_p V_p \frac{d\mathbf{U}_p}{dt} \approx -\rho_f \sum_{l=1}^{N_L} \mathbf{F}_l \Delta V_l + \rho_f \frac{d}{dt}\left(\int_{V_p} \mathbf{u}dV\right)$$
$$+ \int_{V_p} (\rho_p - \rho_B)\mathbf{g} + \mathbf{F}_c, \tag{12}$$

for the linear momentum and

$$\frac{d(\mathbf{I}_p \boldsymbol{\Omega}_p)}{dt} \approx -\rho_f \sum_{l=1}^{N_L} \mathbf{r}_l \times \mathbf{F}_l \Delta V_l + \rho_f \frac{d}{dt}\left(\int_{V_p} \mathbf{r} \times \mathbf{u}dV\right)$$
$$- \int_{V_p} \mathbf{r} \times \rho_B \mathbf{g} + \mathbf{T}_c, \tag{13}$$

for the angular velocity.

The first terms on the right-hand-side of the equations above describes the *IBM* force and torque as the summation of all the point forces $\mathbf{F}_l$ on the surface of the particle, the second terms account for the inertia of the fictitious fluid phase trapped inside the particle and the third terms consider the correction due to applying the buoyancy force to the whole computational domain (including the fictitious fluid phase trapped inside the particle). $\mathbf{F}_c$ and $\mathbf{T}_c$ are the force and the torque due to the particle-particle/wall interactions. When the distance between particles (or a particle and a wall) are smaller than one Eulerian grid size, the lubrication force is under-predicted by the *IBM*. To compensate for this inaccuracy and to avoid computationally expensive grid refinements, a lubrication model based on the asymptotic analytical expression for the normal lubrication force between unequal spheres ([34]) is used; here we approximate the two spheroidal particles with two spheres with same mass and radius corresponding to the local curvature at the points of contact. Using these approximating spheres, a soft-sphere collision model with Coulomb friction takes over the interaction when the particles touch. In the current study, only single particles are investigated in a numerical domain without walls, therefore $\mathbf{F}_c$ and $\mathbf{T}_c$ vanish in the equations above. However, the numerical algorithm is designed to capture these solid-solid interactions. More details about the interaction models and validations can be found in [20] and [35]. Eqs. (12) and (13) are integrated in time with the same Runge-Kutta method used for the Navier–Stokes equations.

2.3. Flow configuration

In the present work, we investigate the effect of heat transfer on the sedimentation of isolated particles with different shapes:
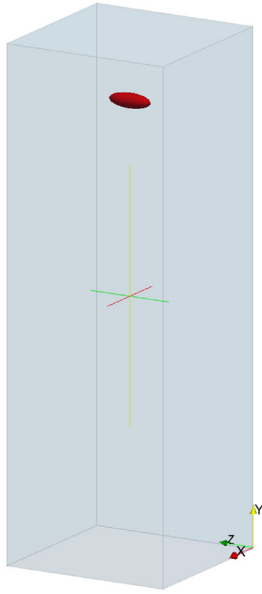
Fig. 1. Schematic of the flow configuration with a single prolate particle falling in the computational domain.

Fig. 2. Time variation of the settling velocity for an isolated sphere falling in an enclosure at various Reynolds numbers against the experimental data of TenCate et al. [42] and the numerical results of Wachs [11].

sphere, oblate spheroids (aspect ratio 1/3) and prolate (aspect ratio 3). Various parameters such as the drag coefficient and the terminal velocity are studied and compared for different shapes at different Grashof and Galileo numbers. A numerical domain of $12D_{eq} \times 24D_{eq} \times 12D_{eq}$ is considered in the *x, y* and *z* directions with gravity acting in the negative *y* direction. D_{eq} is the particle equivalent diameter, computed from the diameter of a sphere with the same volume as the ellipsoidal particle. A semi-infinite boundary condition is considered in the *y* direction, modelled by a finite computational domain that moves with the particle and ensures that the particle is always located at a certain distance from the bottom of the computational box. This method forces the center of the particle to displace only within one Eulerian grid cell, as the particle and the flow field translate one grid cell upwards whenever the particle crosses the bottom boundary of this specified Eulerian grid cell. Since the quiescent fluid, far from the particle (at the bottom of the computational box), is undisturbed by the particle motion, an inflow boundary condition with zero velocity is considered at the bottom together with an outflow condition at the top boundary. Employing these boundary conditions allows for the translation of the grid upwards and updating it with zero velocity at the bottom of the box, whenever the particle crosses the specified grid cell, without creating any discontinuity in the fluid and in the particle motion. More details on this treatment can be found in [3,36,37]. Periodic boundary conditions are considered in the directions, perpendicular to the gravity. A schematic of the flow configuration is demonstrated in Fig. 1. The spheroid aspect ratio $\mathcal{AR}$ is defined as the ratio of the polar symmetric semi-axis *a* to the equatorial radius *b* and D_{eq}, the characteristic length is obtained as:

$$D_{eq} = 2\left(ab^2\right)^{1/3}. \tag{14}$$

A grid resolution of 32 grid cells per D_{eq}, similar to Ardekani et al. [20], Fornari et al. [21], is used for all simulations and particle aspect ratios $\mathcal{AR}$. It should be noted that the thickness of the momentum and the temperature boundary layers can be estimated from $D_{eq}/\sqrt{Re}$ and $D_{eq}/\sqrt{RePr}$, respectively [38]. Therefore, a grid resolution of 32 grid cells per D_{eq} is adequate to fully resolve both boundary layers within the parameter space considered here. All spheroidal particles are released in the domain with their major axis perpendicular to the gravity direction, as other initial orien-

tations are not stable for the free moving spheroidal particles, see [39], and the particle eventually falls with the mentioned stable orientation. ρ_r and Pr are set to 1.1 and 1 in all simulations.
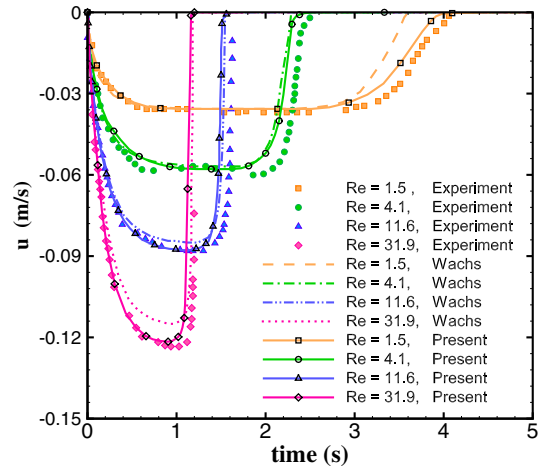
3. Validation

Before examining the effect of heat transfer on the settling of rigid particles of different shapes, we validate our results versus other existing data in the literature. As there is no available experimental and numerical data on the 3*D* thermal convection around non-spherical particles during sedimentation, the settling of spherical particles is considered for the validation of the present work in the two different cases of isothermal and non-isothermal fields. Note that the numerical code has been fully validated for the isothermal sedimentation of non-spherical particles [20] and used in previous works on spheroidal particles [21,40,41].

3.1. Isothermal case: settling of a sphere in a closed system

Similar to other numerical simulations in the literature ([11,43–45]), the experimental data of TenCate et al. [42] together with the numerical results of Wachs [11] are chosen to validate the results concerning the hydrodynamic part.

The original experiment [42] consists of an enclosure with the dimension of $100 \times 100 \times 160$ mm in *x, y* and *z* (gravity direction) direction, filled with a viscous fluid. A solid spherical particle with diameter of 15 mm and density of 1120 Kg/m³ is released from the position $(50, 50, 120)$ mm and settles in the negative *z* direction. Various types of silicon-oil fluids with different density and dynamic viscosity are used to vary the Reynolds number in the range $1 - 32$. Here, the 4 different Reynolds numbers of 1.5, 4.1, 11.6, and 31.9 are simulated and the results are depicted in Fig. 2 against the existing data in the literature [11,42]. The grid resolution of these simulations is set to 32 Eulerian grid cells per particle diameter. The results of these test cases in the figure show a good agreement with the existing data.

3.2. Non-isothermal case: sedimentation of a spherical particle with fixed temperature in a semi-infinite channel

Settling spherical particles with constant temperature, as previously studied by Dan and Wachs [3], are considered here to validate the numerical code. Spherical particles sediment in a semi-infinite domain, surrounded by 4 solid walls, where the size of
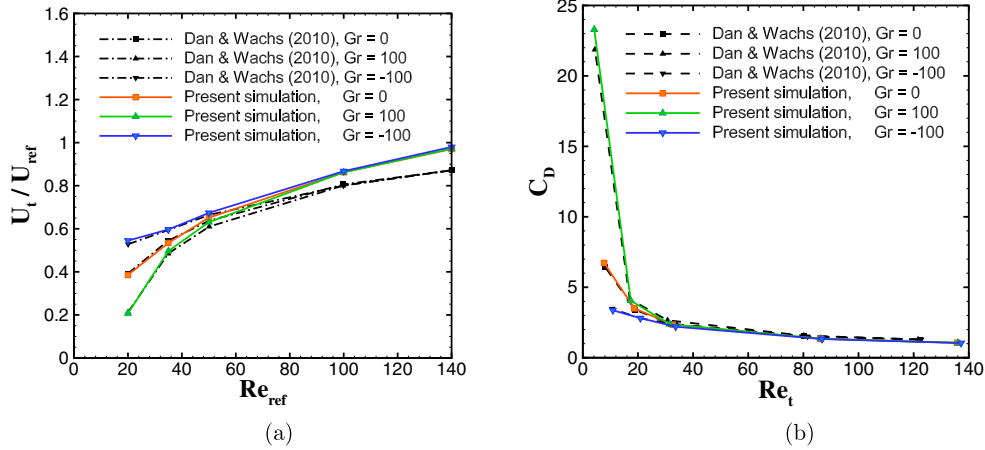
Fig. 3. (a) The terminal velocity U_t, normalized by U_{ref} vs Re_{ref} and (b) the drag coefficient C_D vs Re_t for spherical particles with $Gr = 0$, 100 and -100. The results obtained by Dan and Wachs [3] are indicated with the dashed lines.

the numerical domain in the transverse directions is set to 4 particle diameters. Different cases with the reference Reynolds number ($Re_{ref} \equiv \frac{\rho_f U_{ref} D_{eq}}{\mu}$, where $U_{ref} = \sqrt{\frac{4D}{3}(\rho_r - 1)g}$) varying in the range of $[20 - 140]$ are considered for three different thermal conditions: an isothermal field ($Gr = 0$), a hotter particle ($Gr = 100$) and a colder particle ($Gr = -100$). Pr is set to 1 in these simulations. The terminal velocity U_t, normalized by U_{ref} and the drag coefficient of the particle are depicted in Fig. 3 for various Reynolds numbers and 3 different thermal conditions. The drag coefficient C_D is defined as:

$$C_D = \frac{2F_D}{\rho_f U_t^2 A_s},\tag{15}$$

where F_D denotes the drag force exerted on the particle when it reaches the terminal velocity and A_s is the frontal surface area of the particle. Therefore, it can be shown [46] that:

$$C_D = \frac{U_{ref}^2}{U_t^2}.\tag{16}$$

Fig. 3 shows the comparison of our *IBM* results with that obtained by Dan and Wachs [3]. It is seen that the results of the two methods are in good agreement, providing a validation for the heat transfer algorithm.

4. Results

In this section, we first study the influence of the Grashof number on the settling velocity and the drag coefficient C_D of a single particle with different shapes. Next, we examine the onset of the secondary motion for sedimenting oblate, prolate and spherical particles in the presence of a temperature field.

4.1. Effect of heat transfer on the sedimentation of single spherical and non-spherical particles

Three different thermal conditions are considered here for different shape of settling particles: (a) isothermal field ($Gr = 0$), (b) hotter particle ($Gr = 100$) and (c) colder particle ($Gr = -100$) with Galileo number varying between 10 to 90. The values of the Galileo numbers investigated in this section are chosen below the onset of secondary motion for these particles ([20,47,48]).

Fig. 4 (a)–(c) show the terminal velocities, normalized by U_{ref}, against the Galileo number Ga for the different shapes and different Gr under investigation. The particle settling velocity is observed to increase with respect to the isothermal condition when

Gr is negative (the particle is colder than the surrounding fluid) and to decrease when Gr is positive (the particle is hotter than the surrounding fluid), independently of the shape. This is due to the buoyancy force that increases when Gr is above 0. Interestingly, the results in the panels (a)-(c) indicate a local minimum settling speed for the colder particles around $Ga \approx 30$, regardless of the particle shape. For values below $Ga \approx 30$, the buoyancy force appears stronger than the viscous force, hence enhancing the particle terminal velocity. On the other hand, at larger Galileo numbers ($Ga \approx 90$) the buoyancy effect due to the change in the temperature field is negligible and barely affects the terminal velocity. To show the effect of Gr number on the acceleration or retardation of the cold ($Gr < 0$) and hot ($Gr > 0$) particles, the terminal velocity of these, normalized by their terminal velocity at $Gr = 0$, is depicted in Fig. 4(d) for all shapes considered here. It can be observed that for each particle shape the ratio of the non-isothermal to the isothermal terminal velocity deviates from 1 when the Ga number decreases, implying that the effect of temperature difference on the particle motion is more pronounced at smaller Galileo numbers. It should be noted that Gr/Ga^2 approximates the ratio of the natural convection to the gravitational forces, therefore increasing Ga diminishes the buoyancy effect considerably faster than decreasing Gr. Fig. 4 also indicates that the effect of the Grashof number Gr on the terminal velocity is more pronounced for non-spherical particles (oblates are the most affected). This can be associated with the larger surface area of non-spherical particles, which contributes to an increased heat transfer between the two phases.

The time variation of the particle settling velocity at $Ga = 20$ is depicted in Fig. 5 for different thermal conditions and particle shapes. It can be observed that the steady-state condition is achieved faster in the iso-thermal cases. This can be explained by the slower formation of the temperature wake, which delays the effect of buoyancy forces. Results for the cases with $Gr = 100$ confirms this explanation as the particles experience larger settling velocities initially, before the terminal velocity converges to a smaller value.

The effect of Gr on the particle wake is shown in Fig. 6 for particles with different shapes by means of contours of vertical velocity at settling Reynolds number $Re_t \approx 30$. Indeed, the Galileo number for each case is chosen in such a way that the terminal velocity converges to a similar value. Interestingly, the particle wake appears longer and wider as the Gr changes from -100 in the left column to 100 in the right one. This figure clearly shows how the buoyancy forces lift up the hotter fluid in the vicinity of hot par-
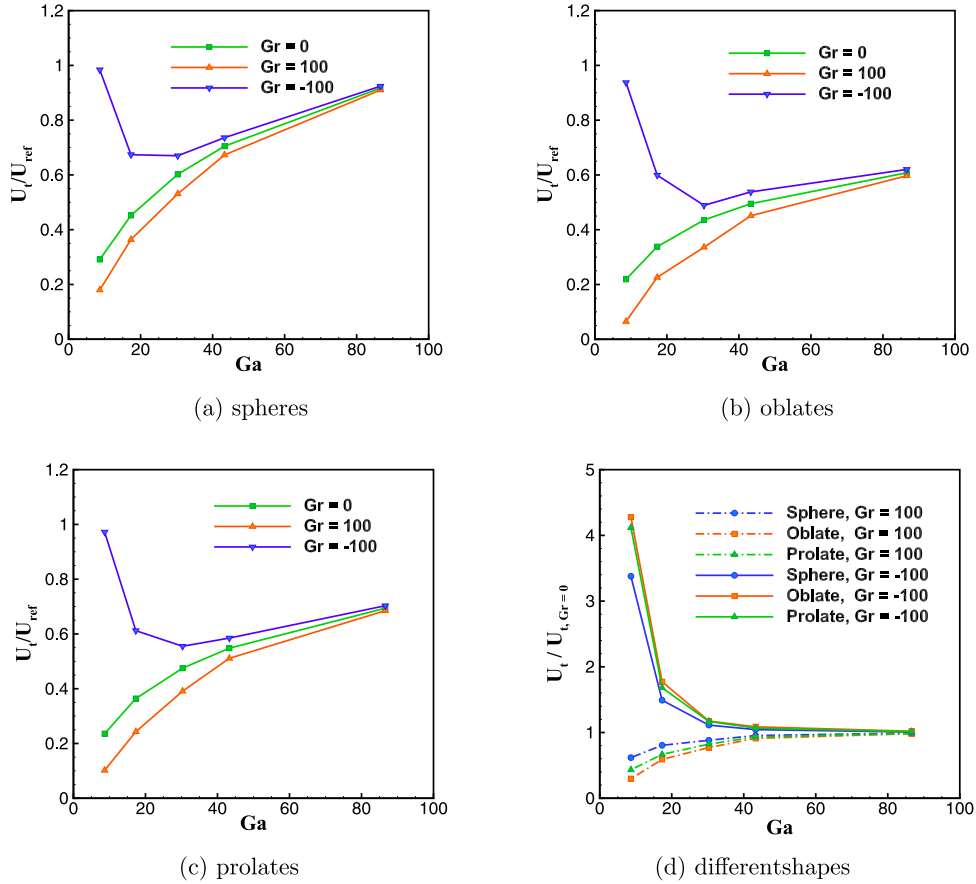
Fig. 4. The particle terminal velocity U_t, normalized by U_{ref} at three values of the Grashof number Gr for (a) spheres, (b) oblates and (c) prolates, and (d) normalized by the corresponding U_t at $Gr = 0$ against the Galileo number Ga for different shapes.
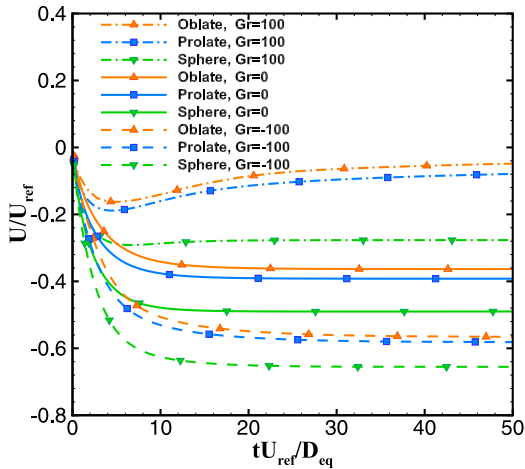
Fig. 5. Time variation of the particle settling velocity for different shapes at $Ga = 20$ and Grashof numbers 100, 0 and -100.

ticles and therefore increase the size of the particle wake with respect to the iso-thermal condition (middle column). The opposite holds when the particle is colder and the buoyancy forces push down the cold fluid, instead, and reduce the wake size. The alteration in the wake size, caused by the buoyancy forces, changes the drag that the particles experience while settling in a viscous fluid, even with the same terminal velocity.

The effects of heat transfer on the drag coefficient C_D of particles with different shapes are depicted in Fig. 7 versus termi-

nal Reynolds number Re_t for the different Gr studied here. The data show that at each Gr and Re_t, oblate particles experience the largest C_D among the different shapes, while the drag coefficient for spheres is the smallest one. This is consistent with the measure of the frontal area as oblates, prolates and spheres have the largest to the smallest frontal area respectively.

Ardekani et al. [20] proposed a simple model to predict the terminal Reynolds number Re_t for spheroidal particles at low Galileo numbers in the case $Gr = 0$. This model assumes that for oblates, spheres and prolate particles the steady flow (wake) regime is similar. The assumption in this model is that for small Galileo numbers, the main effect of a change in spheroid aspect ratio (with respect to a perfect sphere) is the change in the frontal surface area, while the modified C_D remains the same when defining the terminal Reynolds number based on the equivalent sphere diameter D_{eq}. Here we extend this model for non-isothermal conditions, when Gr is not negligible, in order to eliminate the shape effect from the governing parameters. The drag coefficient is therefore computed as follows:

$$C_D = \frac{2 F_D}{\rho_f U_t^2 A_s^*}, \tag{17}$$

where F_D denotes the drag force exerted on the particle in a steady state condition when the particle reaches the terminal velocity. A_s^* is the new frontal area of the particle which can be written as

$$A_s^* = \frac{\pi D_{eq}^2}{4} \mathcal{AR}^n, \tag{18}$$

where D_{eq} is the equivalent diameter of a spherical particle with the same volume and n is equal to $-2/3$, $1/3$ and 0 for oblate, prolate and sphere respectively. Therefore, the new modified C_D is
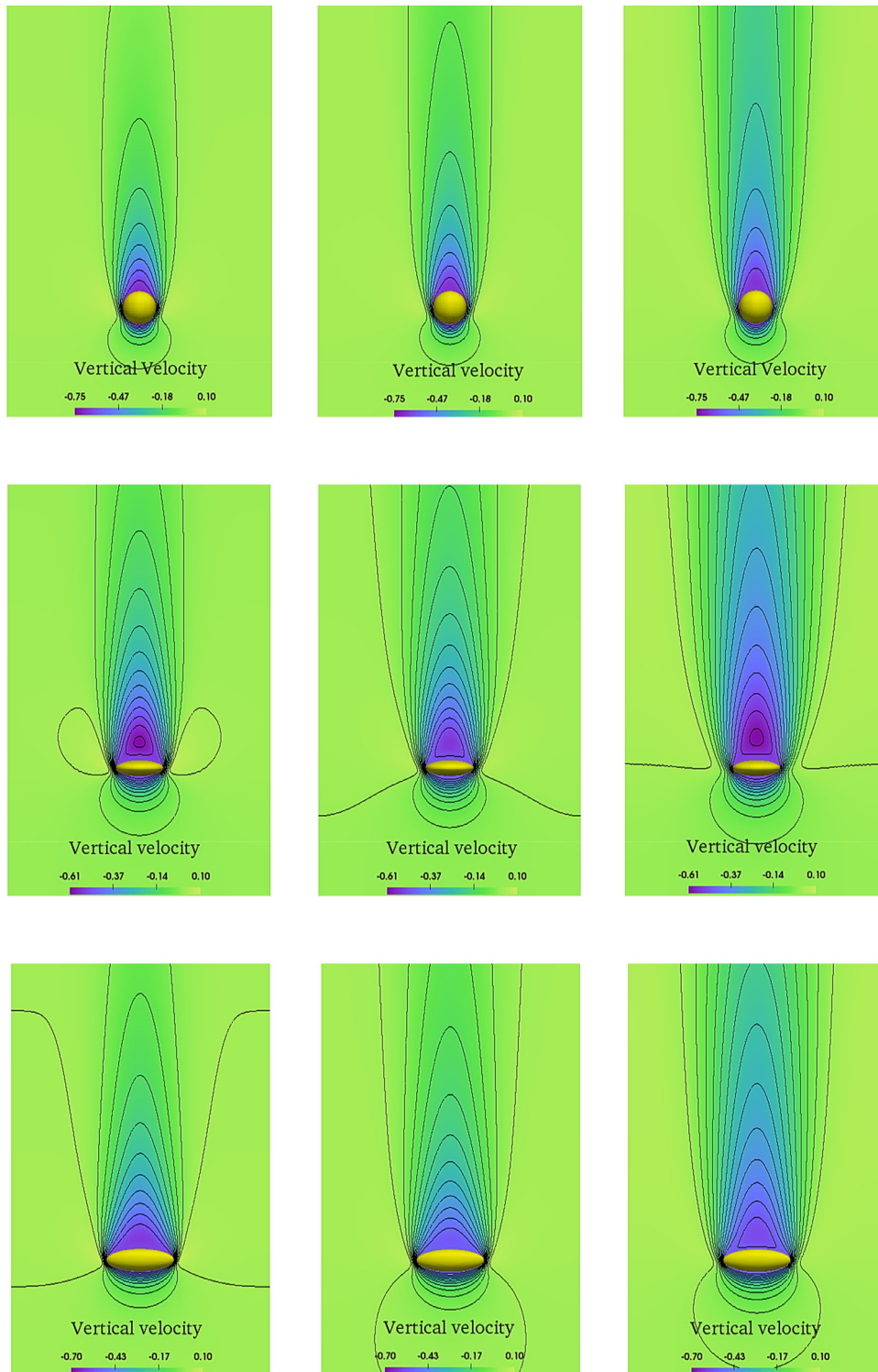
Fig. 6. Contours of vertical velocity, divided by the viscous scale v/D_{eq}, for settling spheroids of aspect ratios $\mathcal{AR} = 1$ (first row), 1/3 (second row) and 3 (the last row). The Grashof number Gr is -100, 0 and 100 from left to right. The Galileo number Ga is chosen in a way to obtain the same terminal Reynolds number of approximately 30.

calculated based on the multiplication of the drag coefficient and $\mathcal{AR}^n$ as:

$$C_D \, \mathcal{AR}^n = \frac{2\,F_D}{\rho_f U_t^2 A_s}, \tag{19}$$

where F_D and A_s are obtained employing D_{eq}. The results of the modified drag coefficient are depicted in Fig. 8 versus the particle terminal Reynolds number for the three studied thermal condi-

tions and particle shapes. The drag coefficient corrected to account for the particle shape, oblate, prolate and sphere, follows a master curve at each Gr, provided Gr/Ga^2 is small. The empirical relation proposed by Clift et al. [49], for the drag coefficient of an isolated sphere is also plotted in this figure: this well collapses on the results of the isothermal cases. The proposed new scaling shows that the shape can be eliminated from the governing parameters below the onset of the particle secondary motion and the drag coef-
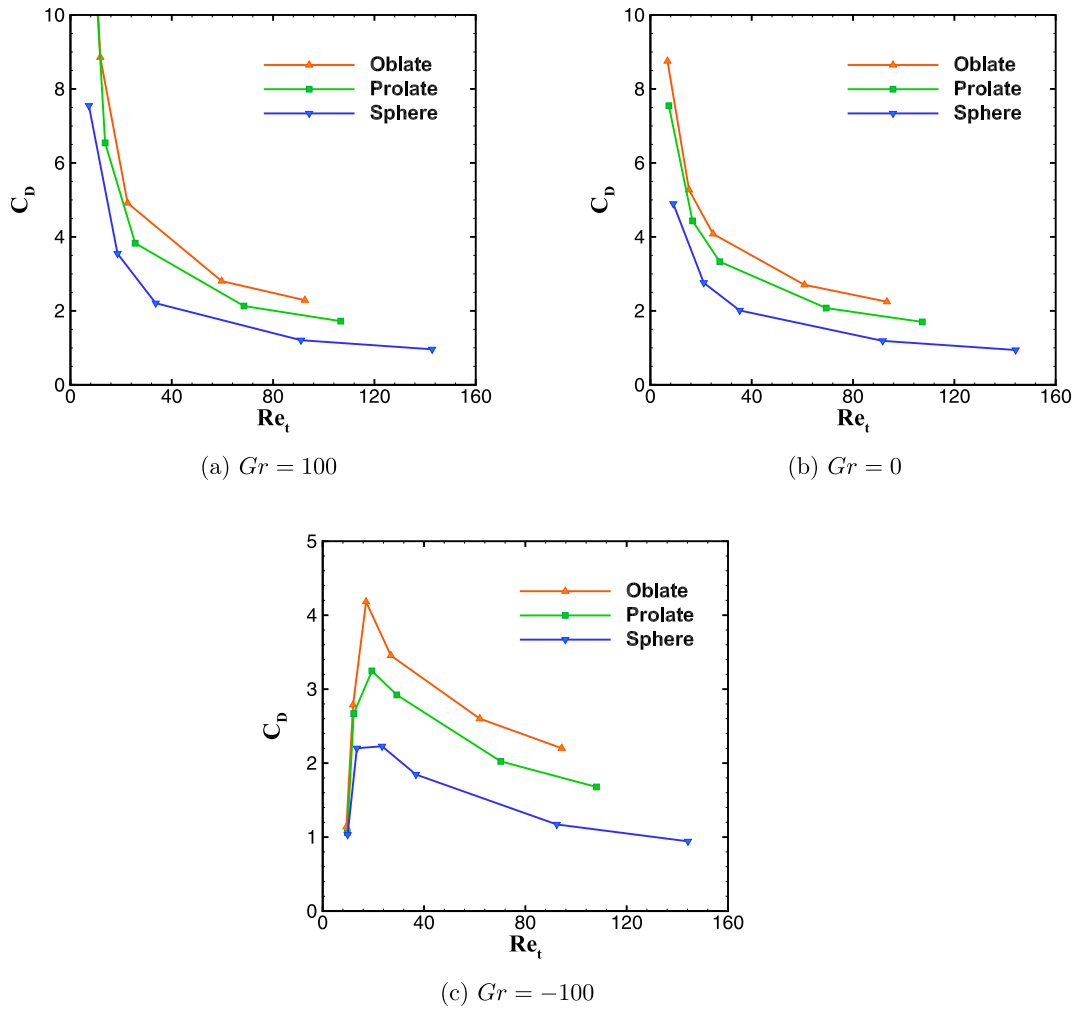
(a) $Gr = 100$

(b) $Gr = 0$

(c) $Gr = -100$

Fig. 7. The drag coefficients of oblate, prolate and spherical particles as a function of terminal Reynolds number Re_t for different thermal conditions of $(a)\, Gr = 100$, $(b)\, Gr = 0$ and $(c)\, Gr = -100$.
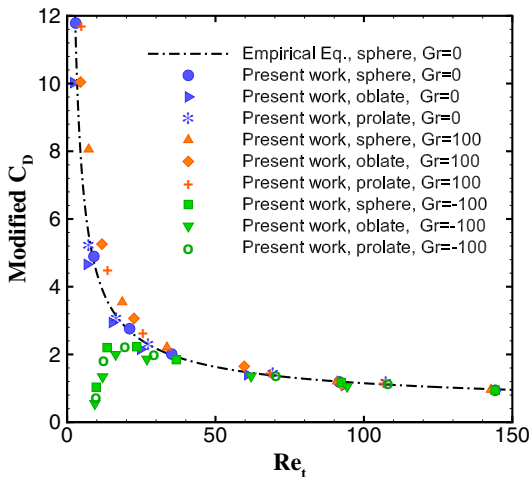
Fig. 8. (Color online) Comparison of the modified drag coefficients (See text) for the three different particle shapes under investigation and various thermal conditions.

ficient for any spheroidal particle can be predicted from the data of settling spheres at the desired Grashof number. This implies that for sufficiently small values of the Galileo number and of the ratio Gr/Ga^2, the particle shape can be parametrised by the frontal area

and the drag coefficient of a spheroid can be estimated from the drag coefficient C_D of a sphere with the same volume as the original spheroid.

4.2. Stability analyzing of single spherical and non-spherical particles in the presence of heat transfer

Jenny et al. [50] performed a parametric study for sedimenting spheres, reporting a diagram of flow regimes in the $Ga - \rho_r$ parameter plane. These authors identified the critical $Ga \approx 155$ for the onset of secondary motion for spheres with similar density ratio as in the present study. Below $Ga \approx 155$ a spherical particle settles steadily on a straight vertical path with an axisymmetric wake, consisting of a single toroidal vortex. Chrust [47] studied the influence of the aspect ratio $\mathcal{AR}$, density ratio ρ_r and Ga on the settling state of oblate particles, indicating four different states for the oblate particle motion. Ardekani et al. [20] revealed that the onset of secondary motion for spheroidal particles occurs at considerably smaller values of Ga: ≈ 120 ($Re_t \approx 92$) for oblate particles with $\mathcal{AR} = 1/3$ and ≈ 70 ($Re_t \approx 55$) for prolate particles with $\mathcal{AR} = 3$. In this section, we investigate the effect of varying Gr on the settling state of isolated oblates ($\mathcal{AR} = 1/3$), prolates ($\mathcal{AR} = 3$) and spheres with fixed temperatures. To this purpose, different combinations of Gr and Ga to identify the region of stable motion (vertical steady path) in the $Ga - Gr/Ga^2$ plane, with Gr/Ga^2 representing the ratio of the natural convection to the grav-

(a) sphere   (b) oblate   (c) prolate
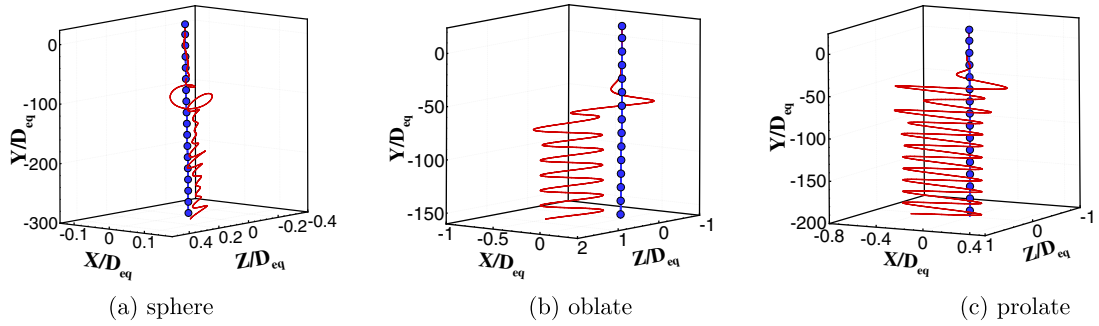
Fig. 9. (Color online) Comparison of the particle trajectory for a (*a*) spherical, (*b*) oblate and (*c*) prolate particle for two different cases of isothermal and non-isothermal flows: $Gr = 0$, $Ga = 60$, blue line with circle scatters and $Gr/Ga^2 = 0.5$, $Ga = 60$, red line.
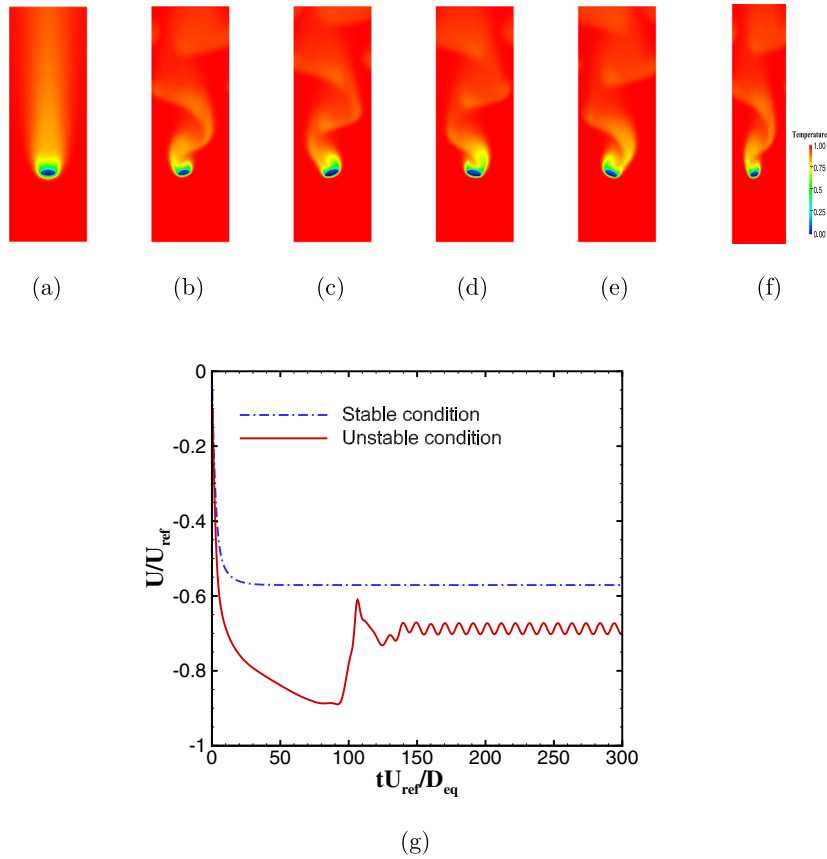
Fig. 10. (Color online) Snapshots of temperature fields for an oblate particle, experiencing a (*a*) stable path ($Gr/Ga^2 = 0.05$, $Ga = 60 : t = 270$), and (*b*) – (*f*) zigzagging motion ($Gr/Ga^2 = 0.5$, $Ga = 60 : t = 250$, $t = 255$, $t = 260$, $t = 265$, $t = 270$). Panel (*g*) indicates the history of the particle settling velocity in the two cases.

itational forces. For this analysis, particles are released from the top of the domain and their paths are tracked for a period of 300 non-dimensional time units ($300D_{eq}/U_{ref}$). Since the particle temperature is kept constant during the time integration, the strong buoyancy of the fluid around the hot particles (positive Grashof number) causes them to reverse the direction of their motion and to move upwards. Therefore, we just study cold particles (negative Grashof numbers) and compare their settling to the iso-thermal cases.

To demonstrate the effect of Grashof number on the particle path, the particle trajectory of the isothermal ($Gr = 0$, $Ga = 60$) cases with different shapes are depicted in Fig. 9 against those of the colder particles ($Gr/Ga^2 = 0.5$, $Ga = 60$). It is observed that the cold particles, under the influence of buoyancy forces, exhibit a path instability at considerably smaller Galileo numbers. There-

fore in addition to the density ratio and the Galileo number, the ratio Gr/Ga^2 is also playing an important role for the particle path stability.

Fig. 10 shows the temperature contours for a falling oblate, where Gr is increased from $Gr/Ga^2 = 0.05$ (10(a)) to $Gr/Ga^2 = 0.5$ in panels (b)-(f). The time history of the settling speed for the two cases is depicted versus time in Fig. 10(g). The data clearly show that the particle stable vertical path observed at low Gr turns into a zigzagging motion with oscillating terminal velocity when Gr increases. Given the definition of U_{ref} in Eq. (6) and Ga in Eq. (5), the terminal Reynolds number can be calculated as below:

$$Re_t = \frac{U_t}{U_{ref}} \frac{2\,Ga}{\sqrt{3}}. \tag{20}$$
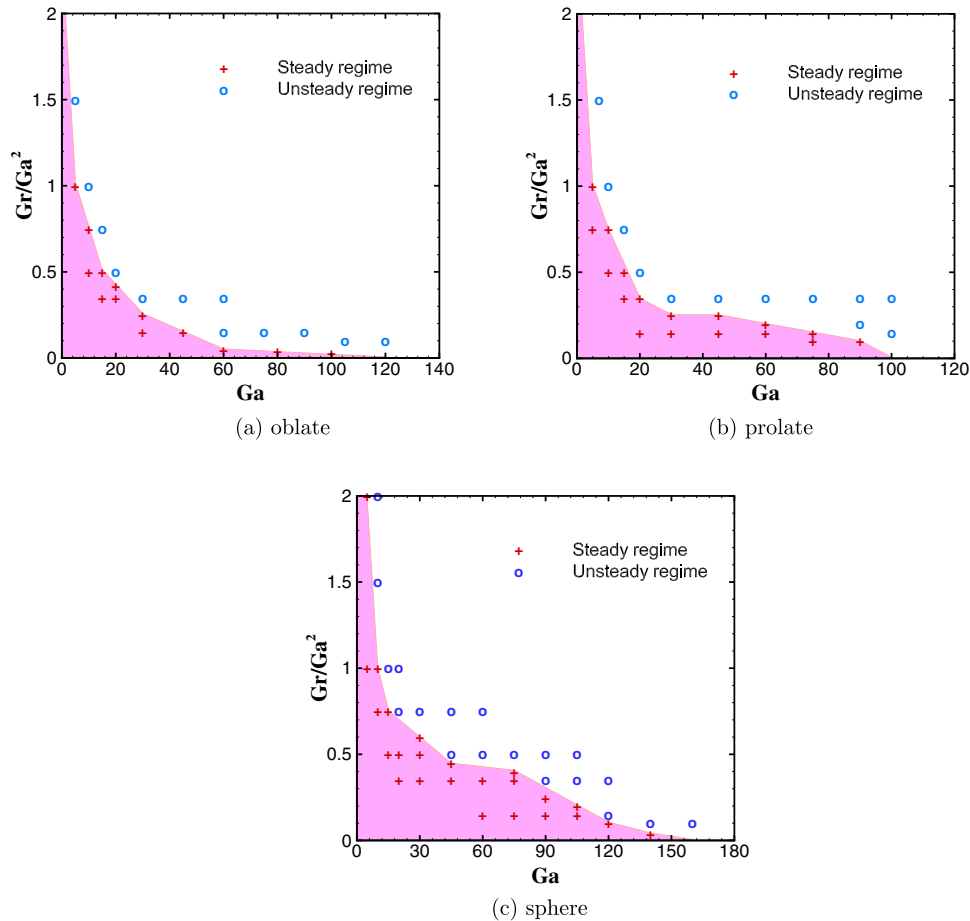
Fig. 11. Diagram of particle settling behaviour in the (Ga, Gr/Ga^2) parameter plane for (a) oblate, (b) prolate and (c) spherical particles settling in an infinite domain. The region where the wake is axisymmetric and the particle trajectory is steady and vertical is indicated by the pink background.

It should be mentioned here that the settling Reynolds number of the 2 cases in Fig. 10 is well below the onset of secondary motion ($Re_t \approx 92$) for iso-thermal oblate particles with $\mathcal{AR} = 1/3$. This implies that buoyancy effects not only increase the particle terminal velocity but also trigger the transition to unsteady settling at Reynolds numbers well below those of iso-thermal particles. This can be observed in Fig. 10(g), where the path instability occurs at $Re \approx 62.35$, before it reaches to the terminal Reynolds number of ≈ 46.5. The path instability is closely related to the wake instability behind the particle [51,52] and the presence of buoyancy forces in the flow can trigger the wake instability at lower terminal Reynolds numbers. Moreover, it is observed in the study of settling spheroids in isothermal flows [20] that the exact value of Ga at which the vortices in the particle wake become unstable depends on the ambient noise, suggesting that there exists a subcritical instability that can be triggered by disturbances in the flow. Motivated by this observation, we have performed a series of additional simulations with different Ga and Gr to identify the onset of unsteady settling: in Fig. 11 we report the regions of stable sedimentation (vertical path) in the $Ga - Gr/Ga^2$ plane. These maps are generated for the 3 particle shapes investigated in this study. The pink color in the figures indicates the region where the particle falls with a straight vertical path. This pink region is considerably larger for the spherical particles than for spheroidal shapes. In other words, the spheroidal particles start the zigzagging motion at considerably lower Ga and Gr/Ga^2. Oblate particles ($\mathcal{AR} = 1/3$) are observed to be the most sensitive shape to varying Gr; i.e. the critical Ga after which the particle exhibits the zigzagging motion

is considerably smaller for oblate particles than for prolates at low Gr/Ga^2. However, the two spheroidal shapes have a similar behavior as Gr/Ga^2 increases beyond 0.5. Another striking finding is that when Ga exceeds the critical value, all particles studied here perform a zigzagging motion. In fact, the oblique wake regime, previously observed for spheres and oblates at $Gr = 0$ [20,50], disappears in the presence of temperature driven buoyancy forces.

5. Final remarks

We have presented results from fully resolved simulations of settling isolated spherical and non-spherical particles with a temperature difference with respect to the surrounding viscous fluid. The particle temperature is assumed constant in this study to avoid additional parameters such as heat capacity and thermal diffusion ratio between the two phases. The discrete forcing immersed boundary method (*IBM*) is employed in this study to represent the fluid-solid interaction in both momentum and temperature equations, while the Boussinesq approximation is used for the coupling of momentum and temperature. The results of our numerical code are first validated against available experimental and numerical data for various cases of isothermal and non-isothermal settling spherical particles.

We first study the influence of the Grashof number on the settling velocity and the drag coefficient C_D of a single spheroidal particle of different aspect ratios. The results of the simulations show that the particle settling velocity increases with respect to the isothermal conditions when Gr is negative (the particle is colder that the surrounding fluid) whereas it decreases when the parti-

cle is hot, i.e. positive Grashof numbers. The ratio Gr/Ga^2, indicating the ratio of the natural convection to the gravitational forces, is found to play an important role in the particle dynamics; in particular, we show that increasing Ga diminishes the buoyancy effect considerably faster than decreasing Gr. This explains why the settling velocity of cold particles at a constant Gr increases when reducing Ga in a sufficiently small range of Galileo numbers ($Gr = -100$ and $Ga < 30$). As regards the particle shape, we show that for any spheroidal particle below the onset of secondary motion, at low Ga and Gr/Ga^2, the drag coefficient can be predicted from that of the settling spheres at the desired Grashof number and the spheroidal particle frontal area: in other words, the main modifications due to the particle shape can be accounted for by the change of the particle frontal area.

Next, we conduct an extensive campaign of simulations with different Ga and Gr in order to identify the areas of stable sedimentation (vertical steady path) and of zigzagging motion in the $Ga - Gr/Ga^2$ plane for the 3 particle shapes investigated in this study. Interestingly, this region is considerably larger for the spherical particles than for spheroidal shapes. Hence, the spheroidal particle settling bifurcates to unsteady motions at considerably lower Ga and Gr/Ga^2. Oblate particles ($\mathcal{AR} = 1/3$) are observed to be the most sensitive to varying Gr; i.e. the critical Ga beyond which the particle exhibits the zigzagging motion is considerably smaller for oblate particles than for prolates at low Gr/Ga^2. However, both spheroidal shapes display a similar behavior as Gr/Ga^2 increases beyond 0.5.

With the behaviour of single particles studied in this work, the next step would therefore be to investigate the sedimentation of a group of non-spherical particles in quiescent and turbulent environments and to address the thermal effects on the global suspension behaviour.

Declaration of Competing Interest

None.

CRediT authorship contribution statement

Mohammad Majlesara: Methodology, Software, Validation, Formal analysis, Writing - original draft. **Omid Abouali:** Conceptualization, Writing - review & editing, Supervision. **Reza Kamali:** Writing - review & editing. **Mehdi Niazi Ardekani:** Conceptualization, Methodology, Software, Writing - review & editing. **Luca Brandt:** Writing - review & editing.

Acknowledgments

References

[1] Z. Yu, X. Shao, A. Wachs, A fictitious domain method for particulate flows with heat transfer, J. Comput. Phys. 217 (2) (2006) 424–452.

[2] Z.-G. Feng, E.E. Michaelides, Inclusion of heat transfer computations for particle laden flows, Phys. Fluids 20 (4) (2008) 040604.

[3] C. Dan, A. Wachs, Direct numerical simulation of particulate flow with heat transfer, Int. J. Heat Fluid Flow 31 (6) (2010) 1050–1057.

[4] F.E. Fendell, Laminar natural convection about an isothermally heated sphere at small Grashof number, J. Fluid Mech. 34 (1) (1968) 163–176.

[5] C. Hieber, B. Gebhart, Mixed convection from a sphere at small Reynolds and Grashof numbers, J. Fluid Mech. 38 (1) (1969) 137–159.

[6] Z.-G. Feng, E.E. Michaelides, Unsteady heat transfer from a sphere at small Peclet numbers, J. Fluids Eng. 118 (1) (1996) 96–102.

[7] E. Bar-Ziv, B. Zhao, E. Mograbi, D. Katoshevski, G. Ziskind, Experimental validation of the Stokes law at nonisothermal conditions, Phys. Fluids 14 (6) (2002) 2015–2018.

[8] J. Comer, C. Kleinstreuer, Computational analysis of convection heat transfer to non-spherical particles, Int. J. Heat Mass Transf. 38 (17) (1995) 3171–3180.

[9] Z.-G. Feng, E.E. Michaelides, Unsteady heat and mass transfer from a spheroid, AlChE J. 43 (3) (1997) 609–614.

[10] H. Gan, J. Chang, J.J. Feng, H.H. Hu, Direct numerical simulation of the sedimentation of solid particles with thermal convection, J. Fluid Mech. 481 (2003) 385–411.

[11] A. Wachs, Rising of 3D catalyst particles in a natural convection dominated flow by a parallel DNS method, Comput. Chem. Eng. 35 (11) (2011) 2169–2185.

[12] Z. Hashemi, O. Abouali, R. Kamali, Three dimensional thermal lattice Boltzmann simulation of heating/cooling spheres falling in a newtonian liquid, Int. J. Therm. Sci. 82 (2014) 23–33.

[13] A. Xu, W. Shyy, T. Zhao, Lattice Boltzmann modeling of transport phenomena in fuel cells and flow batteries, Acta Mech. Sin. 33 (3) (2017) 555–574.

[14] A. Eshghinejadfard, D. Thévenin, Numerical simulation of heat transfer in particulate flows using a thermal immersed boundary lattice Boltzmann method, Int. J. Heat Fluid Flow 60 (2016) 31–46.

[15] H. Tavassoli, E. Peters, J. Kuipers, Direct numerical simulation of fluid–particle heat transfer in fixed random arrays of non-spherical particles, Chem. Eng. Sci. 129 (2015) 42–48.

[16] L. He, D.K. Tafti, Heat transfer in an assembly of ellipsoidal particles at low to moderate Reynolds numbers, Int. J. Heat Mass Transf. 114 (2017) 324–336.

[17] A. Xu, L. Shi, T. Zhao, Thermal effects on the sedimentation behavior of elliptical particles, Int. J. Heat Mass Transf. 126 (2018) 753–764.

[18] K. Walayat, Z. Zhang, K. Usman, J. Chang, M. Liu, Dynamics of elliptic particle sedimentation with thermal convection, Phys. Fluids 30 (10) (2018) 103301.

[19] W.-P. Breugem, A second-order accurate immersed boundary method for fully resolved simulations of particle-laden flows, J. Comput. Phys. 231 (13) (2012) 4469–4498.

[20] M.N. Ardekani, P. Costa, W.P. Breugem, L. Brandt, Numerical study of the sedimentation of spheroidal particles, Int. J. Multiphase Flow 87 (2016) 16–34.

[21] W. Fornari, M.N. Ardekani, L. Brandt, Clustering and increased settling speed of oblate particles at finite Reynolds number, J. Fluid Mech. 848 (2018) 696–721.

[22] W. Fornari, S. Zade, L. Brandt, F. Picano, Settling of finite-size particles in turbulence at different volume fractions, Acta Mech. (2019) 1–18.

[23] M.N. Ardekani, O. Abouali, F. Picano, L. Brandt, Heat transfer in laminar Couette flow laden with rigid spherical particles, J. Fluid Mech. 834 (2018) 308–334.

[24] M.N. Ardekani, L. Al Asmar, F. Picano, L. Brandt, Numerical study of heat transfer in laminar and turbulent pipe flow with finite-size spherical particles, Int. J. Heat Fluid Flow 71 (2018) 189–199.

[25] M. Uhlmann, An immersed boundary method with direct forcing for simulation of particulate flow, J. Comput. Phys. 209 (2) (2005) 448–476.

[26] T. Kempe, J. Fröhlich, An improved immersed boundary method with direct forcing for the simulation of particle laden flows, J. Comput. Phys. 231 (9) (2012) 3663–3684.

[27] M. Niazi Ardekani, Numerical Study of Transport Phenomena in Particle Suspensions, KTH Royal Institute of Technology, 2019 Ph.D. thesis.

[28] R.A. Lambert, F. Picano, W.-P. Breugem, L. Brandt, Active suspensions in thin films: nutrient uptake and swimmer motion, J. Fluid Mech. 733 (2013) 528–557.

[29] K. Sugiyama, S. Ii, S. Takeuchi, S. Takagi, Y. Matsumoto, A full Eulerian finite difference approach for solving fluid–structure coupling problems, J. Comput. Phys. 230 (3) (2011) 596–627.

[30] D. Izbassarov, M.E. Rosti, M.N. Ardekani, M. Sarabian, S. Hormozi, L. Brandt, O. Tammisola, Computational modeling of multiphase viscoelastic and elasto-viscoplastic flows, Int. J. Numer. Methods Fluids 88 (2018) 521–543.

[31] P. Wesseling, Principles of Computational Fluid Dynamics, vol. 29, Springer Science & Business Media, 2009.

[32] A.M. Roma, C.S. Peskin, M.J. Berger, An adaptive version of the immersed boundary method, J. Comput. Phys. 153 (2) (1999) 509–534.

[33] K. Luo, Z. Wang, J. Fan, K. Cen, Full-scale solutions to particle-laden flows: multidirect forcing and immersed boundary method, Phys. Rev. E 76 (6) (2007) 66709.

[34] D. Jeffrey, Low-Reynolds-number flow between converging spheres, Mathematika 29 (1) (1982) 58–66.

[35] P. Costa, B.J. Boersma, J. Westerweel, W.-P. Breugem, Collision model for fully resolved simulations of flows laden with finite-size particles, Phys. Rev. E 92 (5) (2015) 53012.

[36] Z. Yu, N. Phan-Thien, Y. Fan, R.I. Tanner, Viscoelastic mobility problem of a system of particles, J. Non-Newtonian Fluid Mech. 104 (2–3) (2002) 87–124.

[37] A. Wachs, A DEM-DLM/FD method for direct numerical simulation of particulate flows: sedimentation of polygonal isometric particles in a newtonian fluid with collisions, Comput. Fluids 38 (8) (2009) 1608–1628.

[38] A. Doostmohammadi, S. Dabiri, A.M. Ardekani, A numerical study of the dynamics of a particle settling at moderate Reynolds numbers in a linearly stratified fluid, J. Fluid Mech. 750 (2014) 5–32.

[39] P. Ern, F. Risso, D. Fabre, J. Magnaudet, Wake-induced oscillatory paths of bodies freely rising or falling in fluids, Annu. Rev. Fluid Mech. 44 (2012) 97–121.

[40] M.N. Ardekani, P. Costa, W.P. Breugem, F. Picano, L. Brandt, Drag reduction in turbulent channel flow laden with finite-size oblate spheroids, J. Fluid Mech. 816 (2017) 43–70.

[41] M.N. Ardekani, L. Brandt, Turbulence modulation in channel flow of finite-size spheroidal particles, J. Fluid Mech. 859 (2019) 887–901.

[42] A. Ten Cate, C. Nieuwstad, J. Derksen, H. Van den Akker, Particle imaging velocimetry experiments and Lattice-Boltzmann simulations on a single sphere settling under gravity, Phys. Fluids 14 (11) (2002) 4012–4025.

[43] N.G. Deen, S.H. Kriebitzsch, M.A. van der Hoef, J. Kuipers, Direct numerical simulation of flow and heat transfer in dense fluid–particle systems, Chem. Eng. Sci. 81 (2012) 329–344.

[44] Z.-G. Feng, E.E. Michaelides, Robust treatment of no-slip boundary condition and velocity updating for the Lattice-Boltzmann simulation of particulate flows, Comput. Fluids 38 (2) (2009) 370–381.

[45] J. Xia, K. Luo, J. Fan, Simulating heat transfer from moving rigid bodies using high-order ghost-cell based immersed-boundary method, Int. J. Heat Mass Transf. 89 (2015) 856–865.

[46] R. Glowinski, T.-W. Pan, T.I. Hesla, D.D. Joseph, A distributed lagrange multiplier/fictitious domain method for particulate flows, Int. J. Multiphase Flow 25 (5) (1999) 755–794.

[47] M. Chrust, Etude Numérique de la Chute Libre d'Objets Axisymétriques Dans un Fluide Newtonien, Strasbourg, 2012 Ph.D. thesis.

[48] M. Uhlmann, J. Dušek, The motion of a single heavy sphere in ambient fluid: a benchmark for interface-resolved particulate flow simulations with significant relative velocities, Int. J. Multiphase Flow 59 (2014) 221–243.

[49] R. Clift, J.R. Grace, M.E. Weber, Bubbles, Drops, and Particles, Courier Corporation, 2005.

[50] M. Jenny, J. Dušek, G. Bouchet, Instabilities and transition of a sphere falling or ascending freely in a newtonian fluid, J. Fluid Mech. 508 (2004) 201–239.

[51] G. Mougin, J. Magnaudet, Path instability of a rising bubble, Phys. Rev. Lett. 88 (1) (2001) 14502.

[52] B. Yang, A. Prosperetti, Linear stability of the flow past a spheroidal bubble, J. Fluid Mech. 582 (2007) 53–78.